INSTITUT DE FRANCE
Académie des sciences

Comptes Rendus

Mécanique

Mohammad Dehghani, Alireza Shafiei and Mohammad Mahdi Abootorabi

Analyzing orthogonal cutting process using SPH method by kinematic cutting tool

Volume 348, issue 2 (2020), p. 149-174

Published online: 24 June 2020

https://doi.org/10.5802/crmeca.6

Les Comptes Rendus. Mécanique *sont membres du Centre Mersenne pour l'édition scientifique ouverte*
www.centre-mersenne.org
e-ISSN : 1873-7234

Comptes Rendus
Mécanique
2020, 348, nº 2, p. 149-174
https://doi.org/10.5802/crmeca.6

Analyzing orthogonal cutting process using SPH method by kinematic cutting tool

Mohammad Dehghani [a], **Alireza Shafiei** [a] *, **and Mohammad Mahdi Abootorabi** [a]

[a] Department of Mechanical Engineering, Yazd University, Yazd, Iran.

E-mail: arshafiei@yazd.ac.ir (A. Shafiei).

Abstract. In this paper, the orthogonal cutting process is studied using Smooth Particle Hydrodynamic (SPH) method by a kinematic rigid cutting tool and two work-piece material models: perfectly elastic-plastic (EPP) model and Johnson–Cook (JC) model. The kinematic tool means that if the cutting tool is assumed a rigid body then the horizontal component speed of work-piece particles at cutting tool region are modified to the cutting speed. The chip shapes of orthogonal cutting process using SPH method with kinematic and kinetic tool models are compared with the experimental results. The chip obtained by the simulation with kinematic tool is more similar to the experimental results. Von-Mises stress distribution at different states of the orthogonal cutting process is investigated. The maximum stress occurs at the shear plane and causes the formation of chip teeth. Comparisons between chips of work-pieces with two material models are investigated including different rake angles of 5, 10 and 17.5° with feed rates of 0.3 and 0.4 mm/rev and the cutting forces of the process are obtained. The cutting force of process with 17.5° rake angle, 0.4 mm/rev feed rate and 800 m/min cutting speed is validated using experimental result.

Keywords. Orthogonal cutting process, Kinematic and kinetic cutting tool, Johnson–Cook material model, SPH method.

Manuscript received 2nd September 2019, revised 5th November 2019 and 27th November 2019, accepted 28th November 2019.

1. Introduction

Modelling pressure and friction between the traditional kinematic cutting tool and work-piece affect chip morphology, temperature distribution and cutting force in the simulation of orthogonal cutting process. Based on past researches, the coefficient of friction [1,2] is related to pressure distribution along the tool's rake face [3–5] and sliding velocity [6]. Cakir *et al.* [7] studied sticking and sliding friction zones on the rake face while the normal pressure along the sliding length is based on Coulomb friction law.

The finite element method (FEM) is an effective numerical method in the simulation of orthogonal cutting process. A 2-D orthogonal cutting model with plane strain assumption was simulated using Abaqus/Explicit software by Coulomb's friction law [8]. A combined Coulomb–Tresca friction law is used in commercial finite element software (FORGE 2005s) [9] to solve the

* Corresponding author.

thermo-mechanical model of orthogonal cutting process. Furthermore Maranhao *et al.* [10] simulated the thermo-mechanical treatment of machining AISI 316 stainless steel using commercial software Advantedge™ by assuming Coulomb friction coefficient equals to 0.89, 0.80 and 0.53. Tang *et al.* [11] calibrated the FE model based on the comparison between experimental and simulated resultant forces. Wan *et al.* [12] studied the influence of friction models on the formation of dead metal zone (DMZ) using FE method ABAQUS/Explicit software with wide range of friction coefficients. The DMZ is formed under the tool edge and acts as a new cutting edge to prevent the tool edge from wear and affect the roughness of the machined surface. Menezes *et al.* [13] analysed the effect of friction, cutting velocity and rake angle on the cutting forces and chip formation during orthogonal cutting using an explicit finite element method in LS-DYNA. The cutting force varies significantly with rake angle and friction coefficient in comparison with velocity. However, large deformations and material separation are the popular difficulties of the FEM [14–18].

Jaspers *et al.* [19] developed a finite difference model to compute the interface temperature between chip and tool. They measured this temperature using an infrared camera during experimental tests. Gu *et al.* [20] studied dynamic recrystallization phenomenon and thermal conductivity of high-speed machining of Ti6Al4V using material point method (MPM). The friction coefficient is selected to be 0.7. The SPH method can handle the difficulties of FEM such as large deformation and separation of material. Deformation of cutting tool relative to work-piece is very small; therefore, the cutting tool and work-piece can be analysed using FE and SPH methods respectively. This modelling is done using LS-PREPOST pre-processor [21–24] of the company LSTC [25]. The interaction between the cutting tool and work-piece is modelled using friction model. Niu *et al.* [26] simulated orthogonal cutting process of A2024-T351 with an improved SPH method. The improved SPH method is achieved by density and kernel gradient corrections. In these mentioned researches, the coefficient of friction between cutting tool and the work-piece affects the results such as cutting force and chip shape.

In this paper, the orthogonal cutting process is studied using SPH method with a kinematic tool. The kinetic reactions of traditional cutting tool surface as normal and friction forces are replaced with kinematic reactions as normal and tangential velocities at cutting surface. The chip shapes of orthogonal cutting process using SPH method with kinematic and kinetic cutting tool models and two work-piece material models (EPP and JC model) are compared with experimental and simulated [26] results. Rake angle, feed rate and cutting speed are 15°, 0.3 mm/rev and 60 m/min respectively. The chip shape of the process with kinematic cutting tool model is more similar to the experimental results. Comparisons between the chips obtained from cutting process with two work-piece material models, three different rake angles of 5, 10 and 17.5° and feed rates of 0.3 and 0.4 mm/rev are investigated while the cutting speed is 800 m/min. The cutting force of the process including tools with 5, 10, and 17.5° rake angles and 0.3 and 0.4 mm/rev feed rates are obtained. The cutting force of the process including 17.5° rake angle, 0.4 mm/rev feed rate and 800 m/min cutting speed is validated using experimental result.

2. SPH formulation for solid flows

The Mass and momentum conservation are expressed as (1) and (2) respectively [27]:

$$\frac{d\rho}{dt} = \rho \frac{\partial V_\beta}{\partial X_\beta} \tag{1}$$

$$\frac{dV_\alpha}{dt} = \frac{1}{\rho} \frac{\partial \sigma_{\alpha\beta}}{\partial X_\beta} \tag{2}$$

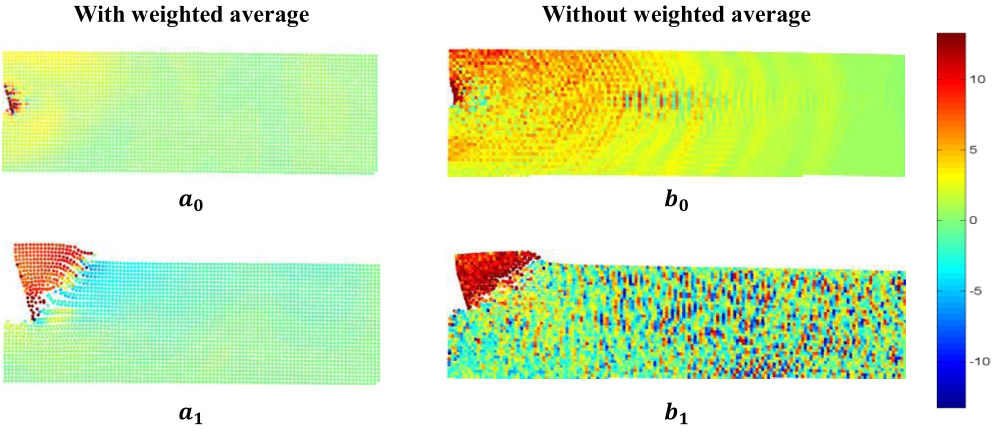

Figure 1. Influence of weight average on velocity distribution.

If $\alpha = \beta = 1,2$ then

$$\begin{aligned} V &= \begin{bmatrix} V_1 & V_2 \end{bmatrix} = \begin{bmatrix} u & v \end{bmatrix} \\ X &= \begin{bmatrix} X_1 & X_2 \end{bmatrix} = \begin{bmatrix} x & y \end{bmatrix} \\ \begin{bmatrix} \sigma_1 & \sigma_{12} \\ \sigma_{12} & \sigma_2 \end{bmatrix} &= \begin{bmatrix} \sigma_x & \sigma_{xy} \\ \sigma_{xy} & \sigma_y \end{bmatrix} \end{aligned} \tag{3}$$

Where ρ, σ, dt, V and X are density, stress, time increment, velocity vector and position vector of particle i.

If the continuum region is divided using SPH particles then the mass and momentum conservation are varied to (3) and (4).

$$\frac{d\rho_i}{dt} = \sum_{j\in\Omega} m_j (V_\beta^i - V_\beta^j) \frac{\partial W_{ij}}{\partial x_\beta} \tag{4}$$

$$\frac{dV_\alpha^i}{dt} = \sum_{j\in\Omega} m_j \left(\frac{\sigma_{\alpha\beta}^i + \sigma_{\alpha\beta}^j}{\rho_i \rho_j} \right) \frac{\partial W_{ij}}{\partial x_\beta} \tag{5}$$

where Ω is integration area, W is kernel function, $W_{ij} = W(x_i - x_j)$, x_i is the place of particle i and x_j is the place of particle j as the neighbour of particle i and m_j and ρ_j are mass and density of particle j.

The speed obtained from (5) is corrected using the weighted average of the neighbouring particles. In other words, at the end of each steps simulation the velocity of particles are replaced by the velocity derived from the weighted average according to the following equation.

$$v^i = \frac{\sum_j^{\text{Neighbor}} w^j v^j}{\sum_j^{\text{Neighbor}} w^j} \tag{6}$$

Figure 1 shows the particles velocity along the cutting speed with/without weighted average velocity. Applying weighted average to the particle velocity makes continues velocity distribution.

In this paper the kernel function is chosen as

$$w = a \begin{cases} 1 - 1.5s^2 + 0.75s^3 & s < 1 \\ 0.25(2-s)^3 & 1 \le s < 2 \\ 0 & s \ge 2 \end{cases} \tag{7}$$

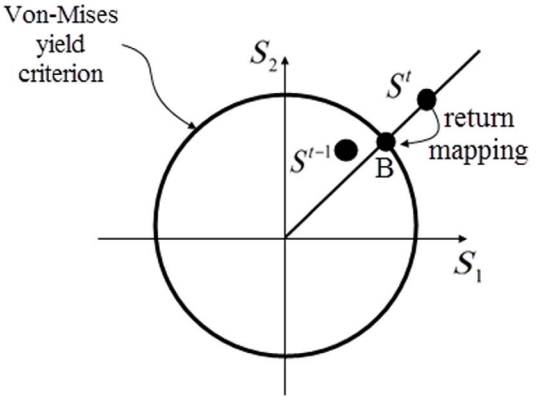

Figure 2. The return mapping algorithm at deviatoric plane stress while the stress of particle *i* is out of the yield condition.

Where

$$\begin{aligned} s &= \frac{r}{H} \\ r &= \sqrt{\left(x_i - x_j\right)^2 + \left(y_i - y_j\right)^2} \\ H &= \frac{h_i + h_j}{2} \end{aligned} \tag{8}$$

Where $a = 10/7\pi h_i^2$, r is minimum distance between two particles and h is smoothing length.

The strain rate at particle *i* is expressed as follow:

$$\dot{\varepsilon}^i_{\alpha\beta} = \frac{1}{2}\left(\frac{\partial V^i_\alpha}{\partial X_\beta} + \frac{\partial V^i_\beta}{\partial X_\alpha}\right) \tag{9}$$

where

$$\frac{\partial V^i_\alpha}{\partial X_\beta} = \sum_{j\in\Omega} \frac{m_j}{\rho_j}\left(V^j_\alpha - V^i_\alpha\right)\frac{\partial W_{ij}}{\partial X_\beta} \tag{10}$$

Energy conservation equation (11) is expressed in particle summation as (12).

$$\frac{de}{dt} = \frac{\sigma^{\alpha\beta}}{\rho}\frac{\partial V^\alpha}{\partial x^\beta} + \dot{Q} \tag{11}$$

$$\frac{de}{dt} = \sum_j m_j \frac{\sigma^i_{\alpha\beta} + \sigma^j_{\alpha\beta}}{\rho_i \rho_j}\left(V^j_\alpha - V^i_\alpha\right)\frac{\partial W_{ij}}{\partial X_\beta} + \dot{Q}_{ij} \tag{12}$$

Where heat flux $\dot{Q}_{ij}$ is calculated from (13) by assuming heat conduction is just between work-piece particles in analysing orthogonal cutting process [27]. The heat conduction between tool and work-piece is denied with respect to the energy transfer in work type.

$$\dot{Q}_{ij} = \sum_j 2k \frac{m_j}{\rho_i \rho_j}\frac{\left(T_j - T_i\right)}{R_{ij}}\frac{\partial W_{ij}}{\partial X_\beta} \tag{13}$$

Where R_{ij} is the distance between two particles and k is coefficient of thermal conductivity. The temperature increment is obtained using the rate of energy as in (14).

$$\Delta T = \frac{de}{dt}\frac{1}{C_p} \tag{14}$$

where C_p is the specific heat of the material.

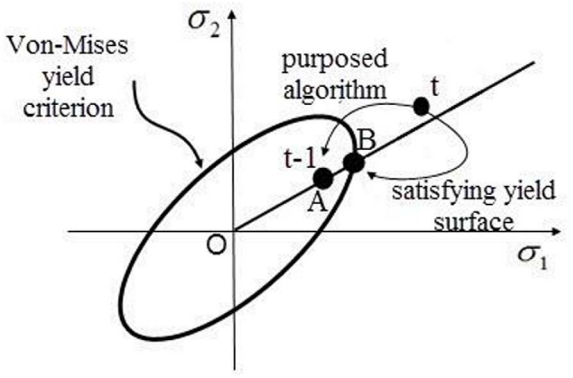

Figure 3. Showing the approximation return mapping algorithm on the main plane stress based on the von Mises yield criterion.

The stress of a particle is obtained from the strain using the Hook's law. If the particle stress satisfies the yield condition ($\sigma_{\text{von}} \geq S_y$) then the particle is in the plastic region of material. In this case, the elastic particle stress is corrected using return mapping algorithm [28] that is shown at Figure 2. In this algorithm the plastic stress is obtained while the following condition is satisfied:

$$\left\| S^t \right\| - \left(2\mu + H\left(\varepsilon_p^i\right)^t\right)\gamma - \sqrt{\frac{2}{3}}\kappa\left(\left(\varepsilon_p^i\right)^t\right) = 0 \tag{15}$$

Where S, μ, H, γ, κ are deviator stress tensor at time t, elastic shear modulus, hardness (the slope of stress-strain diagram at plastic region of a material while $H = 0$ for elastic perfectly plastic material model), plastic consistency parameter and the function of yield stress value that depends on plastic strain respectively.

The amount of γ is obtained from (15) then the stresses are corrected as follows:

$$\left(\sigma^i\right)^t = \left(\sigma^i\right)^t - 2\mu\gamma N \tag{16}$$

Where

$$N = \frac{1}{\left\| S^t \right\|} S^t \qquad \left\| S^t \right\| = \sqrt{2J_2} \tag{17}$$

$$J_2 = \frac{1}{6}\left[\left(\sigma_x - \sigma_y\right)^2 + \left(\sigma_x - \sigma_z\right)^2 + \left(\sigma_z - \sigma_y\right)^2\right] + \sigma_{xy}^2 + \sigma_{xz}^2 + \sigma_{yz}^2 \tag{18}$$

where $\sigma_{xz} = \sigma_{yz} = 0$ in plane strain condition.

In return mapping algorithm, the plastic stresses of particle i exactly satisfies the yield condition. In addition, replacing the stress value at yield moment with the stress at the previous time step according to (19) is suggested.

$$\left(\sigma^i\right)^t = \left(\sigma^i\right)^{t-1} \tag{19}$$

According to Figure 3, if the ellipse is von Mises yield criteria then point (t) is the particle stress at the plastic zone and point ($t-1$) or A represents the step before entering the plastic zone. Point B is obtained by contacting line OA and the ellipse. The line OA represents the loading history of the particle i and point B represents the exact location of stresses at the yield surface. The proposed method assumes that the stresses at the entering the plastic zone is point A instead of the point B to satisfy the yield criterion.

The values of the point A at Figure 3 for each particle at all steps of orthogonal cutting simulation are compared with the value of the point B using relation (20). The maximum errors

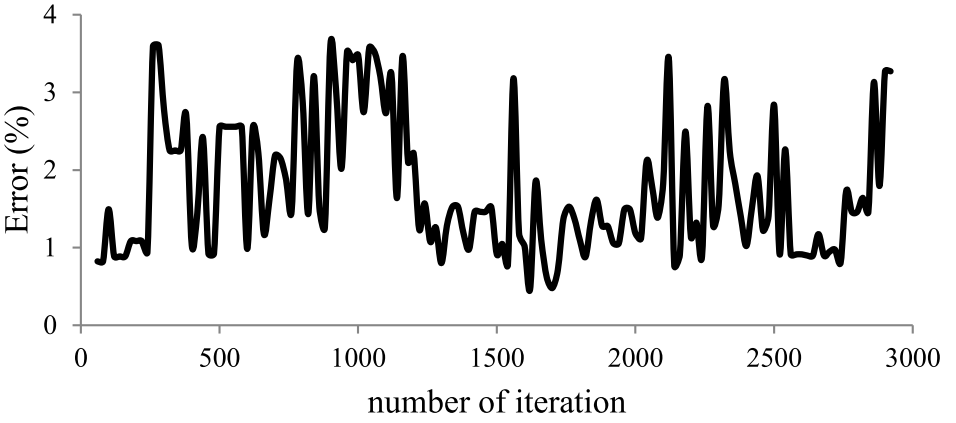

Figure 4. Maximum error of relation (20) among all particles at each time step of the simulation.

between all particles at each time steps are shown at Figure 4. According to Figure 4, the maximum error of approximated stress (point A) is 3.5% with respect to the yield stress (point B). In other words, the radius OB at Figure 3 is reduced with 3.5% for some particles at some simulation steps.

$$\text{Error} = \max\left(\left|\frac{A(\sigma_1) - B(\sigma_1)}{B(\sigma_1)}\right| \times 100, \left|\frac{A(\sigma_2) - B(\sigma_2)}{B(\sigma_2)}\right| \times 100\right) \tag{20}$$

The semi-discrete system is time-stepped with Heun's method, first field variable are predicted with:

$$\begin{aligned}
\left(x^i\right)_p^{n+1} &= \left(x^i\right)^n + \left(u^i\right)^n \Delta t \\
\left(u^i\right)_p^{n+1} &= \left(u^i\right)^n + \left(\frac{du^i}{dt}\right)^n \Delta t \\
\left(\rho^i\right)_p^{n+1} &= \left(\rho^i\right)^n + \left(\frac{d\rho^i}{dt}\right)^n \Delta t \\
\left(\sigma^i\right)_p^{n+1} &= \left(\sigma^i\right)^n + \left(\frac{d\sigma^i}{dt}\right)^n \Delta t
\end{aligned} \tag{21}$$

Where the subscript p designates predicted, the predicted derivatives $\left(du^i/dt\right)_p^{n+1}$, $\left(d\rho^i/dt\right)_p^{n+1}$, $\left(d\rho^i/dt\right)_p^{n+1}$ are then calculated using these values and the final field variables are calculated as:

$$\begin{aligned}
\left(x^i\right)^{n+1} &= \left(x^i\right)_p^{n+1} + \left\{\left(u^i\right)_p^{n+1} - \left(u^i\right)^n\right\} \frac{\Delta t}{2} \\
\left(u^i\right)^{n+1} &= \frac{\left(u^i\right)_p^{n+1} + \left(u^i\right)^n}{2} + \left(\frac{du^i}{dt}\right)_p^{n+1} \frac{\Delta t}{2} \\
\left(\sigma^i\right)^{n+1} &= \frac{\left(\sigma^i\right)_p^{n+1} + \left(\sigma^i\right)^n}{2} + \left(\frac{d\sigma^i}{dt}\right)_p^{n+1} \frac{\Delta t}{2} \\
\left(\rho^i\right)^{n+1} &= \frac{\left(\rho^i\right)^{n+1} + \left(\rho^i\right)^n}{2} + \left(\frac{d\rho^i}{dt}\right)_p^{n+1} \frac{\Delta t}{2}
\end{aligned} \tag{22}$$

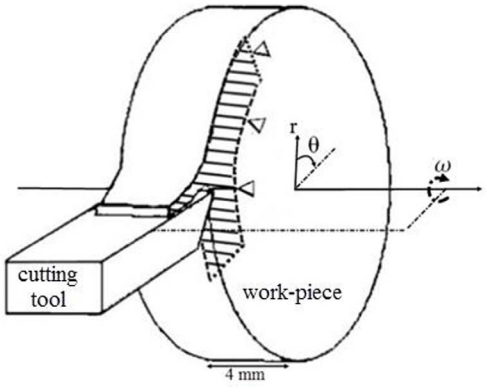

Figure 5. Shaded region is an 2D orthogonal cutting process.

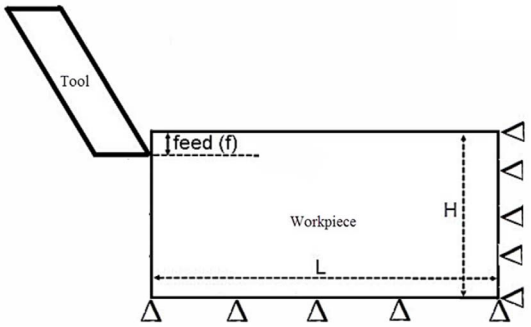

Figure 6. The boundary conditions of orthogonal cutting process.

3. Modelling

Figure 5 shows an orthogonal cutting process while the cutting tool is turning around the work-piece by constant rotational speed (ω). This 3D orthogonal cutting process can be analysed as a 2D model that is shown with the shaded region. The shaded region is repeated through the length of the shaft and the depth of cutting is big in comparison with the feed rate. The cutting tool cuts the work-piece with cutting speed $V_c = r\omega$ through the θ axis where the r represents the distance of tool tip from center of the shaft.

The shaded area of Figure 5 is modelled as Figure 6. In this modelling, the cutting speed is V_c, the dimension of work-piece is $L \times H$ and the feed rate is f mm/rev. The right and down edges of work-piece are fixed along horizontal and vertical direction. The cutting depth is 4 mm according to Figure 5 and the cutting speed of tool tip is 800 m/min.

At Figure 7 the kinematic model is compared with traditional kinetic model while the tool is assumed a rigid body. The cutting tool is advancing to one particle with cutting speed V_c at state (A) while the speed of particle is $V_{\text{particle}} = (u_A, v_A)$. If the particle is at kinematic tool region at state (B) then its horizontal speed is modified to cutting speed $V_{\text{particle}} = (V_c, v_A)$. If the particle is at kinetic tool region at state (B) then the rake face pushes this particle using tangential and vertical forces (F_S and N respectively).

The contact between the particle and traditional kinetic tool occurs when the particle penetrates to the cutting surface of the tool as it is shown at Figure 8. In this contact algorithm the nearest element of the tool surface to the particle is found and the penetration of particle is calcu-

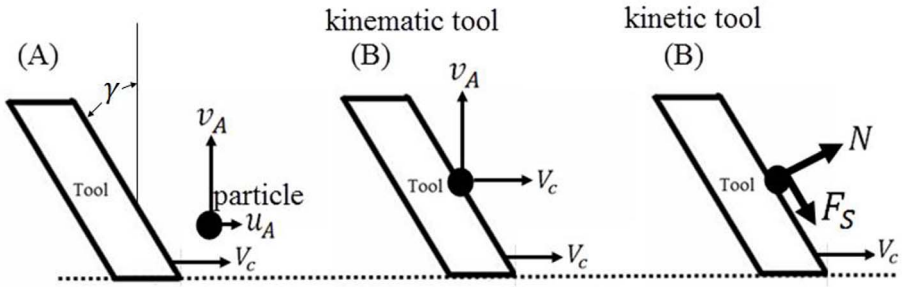

Figure 7. Comparing kinematic and kinetic modelling of cutting tool.

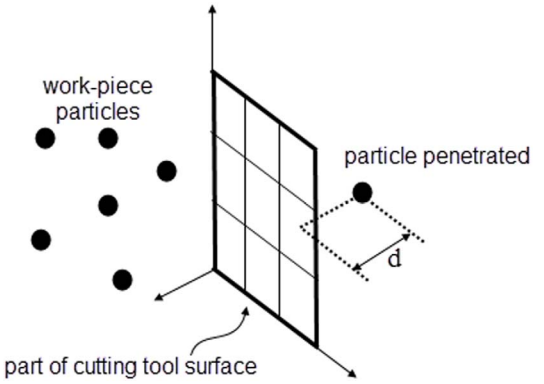

Figure 8. Showing the particle penetration to the cutting tool surface.

lated. A force is applied to the particle according to the relation (23) perpendicular to the surface of the element to reduce this penetration.

$$N = k\left(m^i \frac{d}{\triangle t^2}\right) \tag{23}$$

Where m^i, d, Δt and k are particle mass, amount of penetration, time increment of simulation and coefficient of penetration respectively. The range of k is between zero to 1 while the value of 1 is used to define the rigid body.

By comparing the kinematic and traditional kinetic tool model, the vertical (N) and tangential forces (F_s) to the particle in the kinematic model is obtained as follow:

$$\begin{aligned} N &= m^i \frac{V_c - u^i}{dT}\cos(\gamma) \\ F_s &= \tan(\gamma) N \end{aligned} \tag{24}$$

Where m^i, u^i, dT and γ are particle mass, particle velocity along cutting speed, time increment of simulation and rake angle respectively.

The work-piece of Figure 6 is divided to small area using SPH particles as Figure 9(a) and the region of kinematic cutting tool is plotted using straight lines. Kinetic cutting tool with work-piece are modelled at Figure 9(b) using finite element and SPH particles respectively.

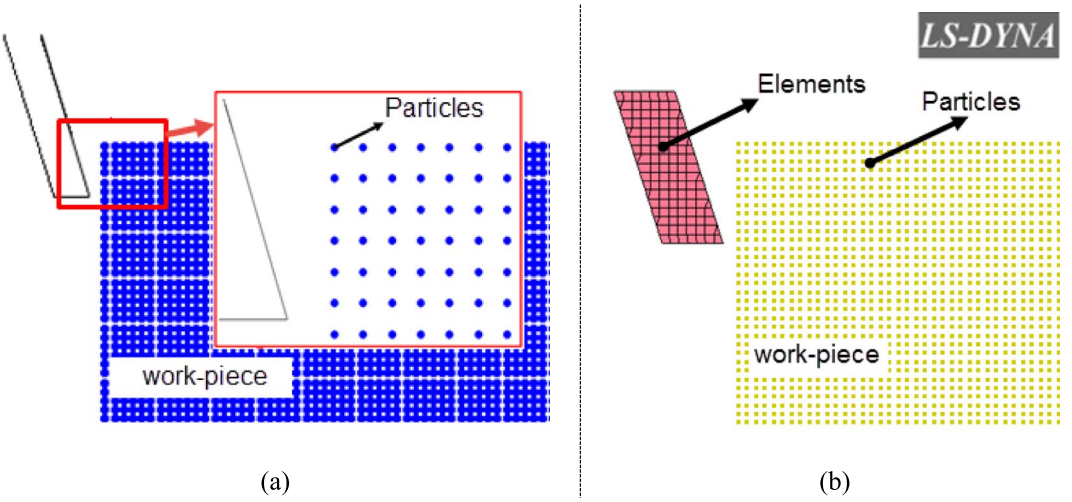

Figure 9. Modelling work-piece using SPH particles with (a) kinematic (b) kinetic models of cutting tool.

3.1. *Material properties*

As a typical ductile material, the aluminium alloy selected was A2024-T351, which is frequently used in the manufacturing processes. In this paper, the von Mises yield criterion is used to identify the critical point of plastic deformation. The von Mises stress (σ_{von}) is compared to the flow yield stress (S_y), and when the criterion ($\sigma_{\text{von}} \geq S_y$) is satisfied, the material enters plastic deformation (flow). EPP and JC material model are applied to model the work-piece material behaviour during the cutting process using SPH method without friction model. The yield stress of EPP material model is:

$$S_y = U \tag{25}$$

Where U is yield strength [29] that is given in Table 1. The yield stress of JC material model is affected by strain hardening, strain rate hardening and thermal softening. The flow stress in the JC model is computed using:

$$S_y = (A + B\bar{\varepsilon}^n)\left(1 + C\ln\left(\frac{\dot{\bar{\varepsilon}}}{\dot{\bar{\varepsilon}}_0}\right)\right)\left(1 - \frac{T - T_{\text{room}}}{T_{\text{melt}} - T_{\text{room}}}\right)^m \tag{26}$$

Where $\bar{\varepsilon}$ is the equivalent plastic strain, $\dot{\bar{\varepsilon}}$ is the plastic strain rate, $\dot{\bar{\varepsilon}}_0$ is the reference strain rate (1.0 s^{-1}), T is temperature, T_{melt} and T_{room} is melt and room temperature respectively. Coefficients of JC model [30] are given in Table 1.

In SPH simulation with Kinetic tool using LS-DYNA software, the JC shear failure model is properly used as Ref [26]. In this software the rake face is divided by the elements and the coefficient of friction is defined at contact element between rake face elements and work-piece particles.

4. Results and discussion

In Figure 10, chip shape of the orthogonal cutting process is obtained using different methods. The cutting speed, rake angle, feed rate and depth of cut are 60 m/min, 15°, 0.3 mm/rev and 4 mm respectively. The colour parts of this figure show the displacements along perpendicular to the cutting speed.

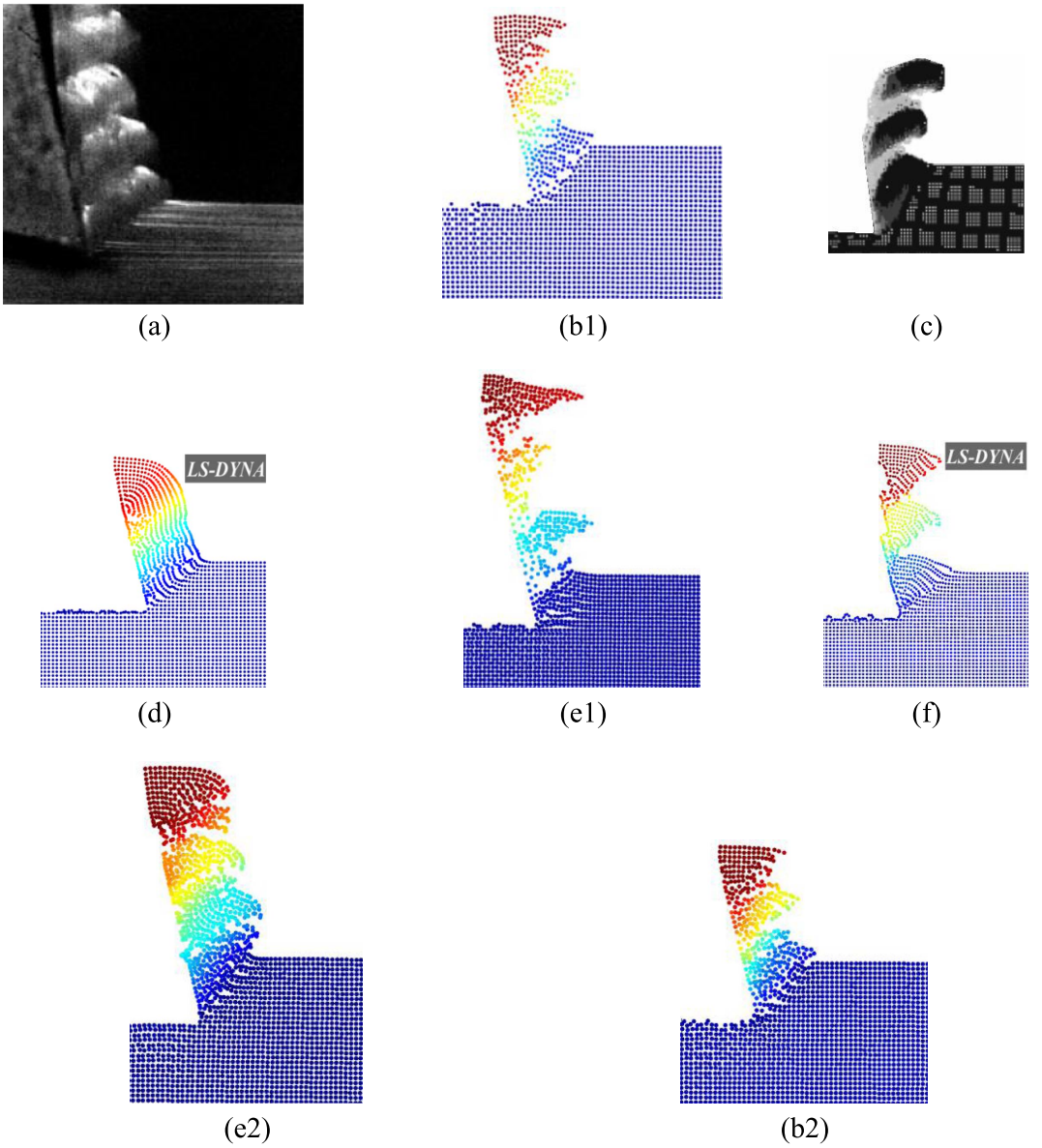

Figure 10. Chip shape of orthogonal cutting process using (a) experimental method [31], (b1) SPH method with kinematic tool including EPP material model using Figure 3 algorithm, (c) SPH method with kinetic tool including JC material model [26], (d) SPH method with kinetic tool including EPP material model by LS-DYNA software, (e1) SPH method with kinematic tool including JC material model using Figure 3 algorithm, (f) SPH method with kinetic tool including JC material model by LS-DYNA software (e2) SPH method with kinematic tool including JC material model using Figure 2 algorithm and (b2) SPH method with kinematic tool including EPP material model using Figure 2 algorithm.

Table 1. Material parameters of A2024-T351 alloy for work-piece [29–31] and uncoated carbide insert CCGX120408-AL, H10 for kinetic cutting tool model [24]

Physical parameter	Work-piece material (A2024-T351)	kinetic tool model
Density, ρ_0 (kg/m^3)	2700	11900
Elastic modulus, E (GPa)	73	534
Poisson's ratio, υ	0.33	0.22
Specific heat, C_p (J/(kg °C))	0.557T+887.6	-
Thermal conductivity, k (w/(m °C))	114	-
Melting temperature, T_{melt} (°C)	520	-
Room temperature, T_{room} (°C)	20	20
Yield strength, U (MPa)	440	
Johnson–Cook material model		
A (MPa)	352	-
B (MPa)	440	-
n	0.42	-
C	0.0083	-
m	1	-

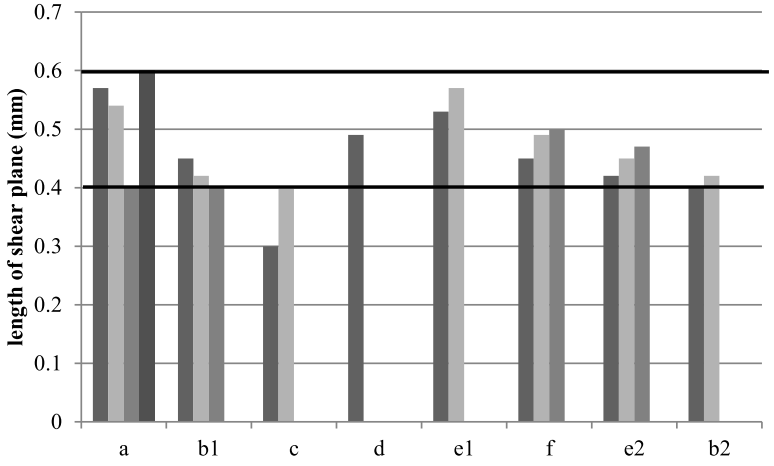

Figure 11. The shear plane length of the chip teeth of Figure 10.

Figure 10(c) is copied from reference [26] that used kinetic cutting tool. The friction force at tool work-piece interface is calculated as multiplication of normal reaction force of tool face and the coefficient of friction. The coefficient of friction in this model is equalled to 0.17.

Chip of Figure 5(d) and (f) are obtained using LS-DYNA software. The rake face is divided by the elements and the coefficient of friction is defined at contact element between rake face elements and work-piece particles. According to [24], Coulomb friction model is used with static (μ_s) and dynamic (μ_d) friction coefficients set to 0.17.

The length of the four teeth of the chip Figure 10(a) is measured, and their values are shown in Figure 11. Also, the lengths of the chip teeth of other Figure 10 parts are included to this figure. According to Figure 11, the lengths of teeth (c) are outside the experimental range (a), and other parts are in the range of part (a). Based on the comparison between the chip shapes (a) to (f) of Figure 10, chip of part (b1), (b2) and (e2) are more similar to the experimental result (a). In addition, part (e1) can correctly predict the shear plane and the shape of the tooth, regardless of the gap between the teeth.

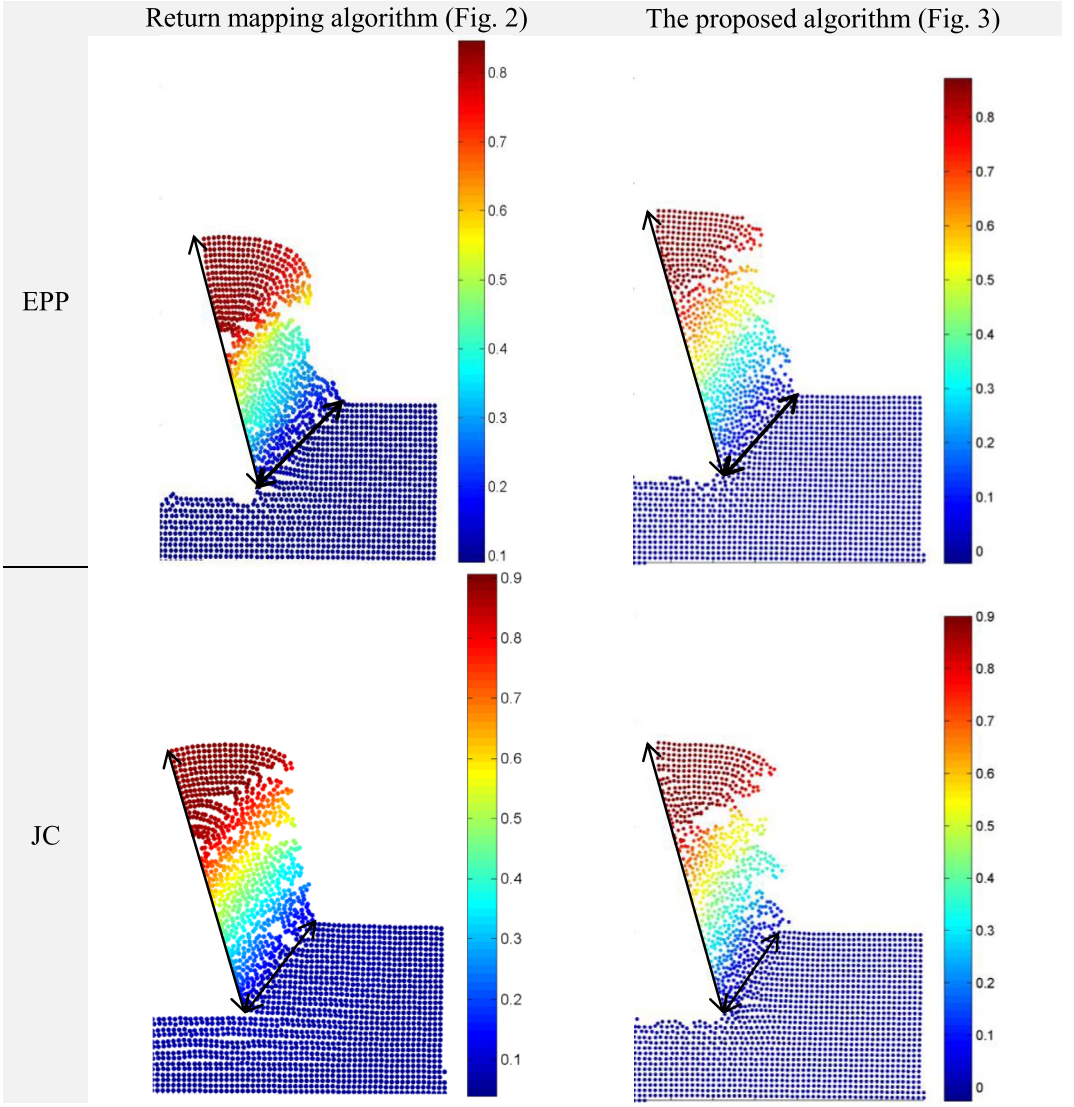

Figure 12. A Comparison of chip shape between the two algorithms presented in Figures 2 and 3.

The chip shapes of the orthogonal cutting process with the kinematic tool using SPH method based on return mapping algorithm (Figure 2) and proposed algorithm (Figure 3) are compared at Figure 12. The work-piece material model is EPP and JC. In this figure, cutting speed, rake angle, feed rate and depth of cut are 800 m/min, 17.5°, 0.4 mm/rev and 4 mm respectively. The length of shear plane and chip are assigned at all parts of this figure and are investigated at Table 2. According to this table, the chips and shear planes length of all parts of Figure 12 are approximately same as others.

The effect of the ratio of the number of particles per work-piece unit area is demonstrated in Figure 13 using kinematic tool and JC material model. In this analysing the feed rate and cutting speed is 0.4 mm/rev and 800 m/min respectively.

According to Figure 13, there are 2, 4, 8, 10, 16 and 20 particles along the feed rate using 25,

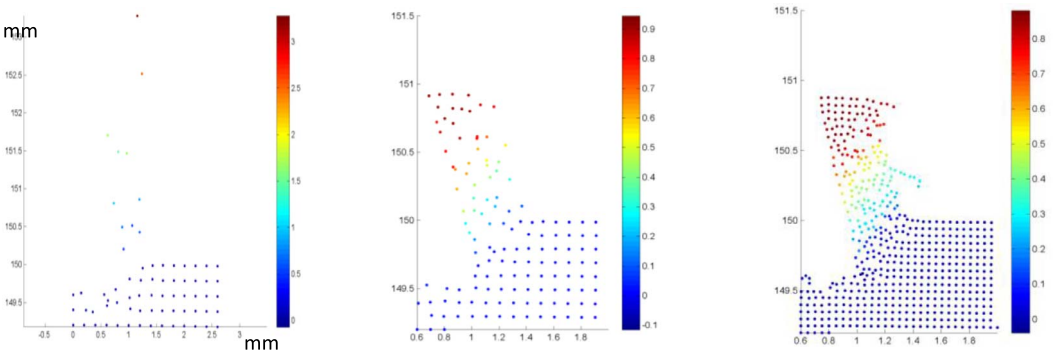

(a) 25 node/mm^2 (b) 100 node/mm^2 (c) 400 node/mm^2

(d) 625 node/mm^2 (e) 1600 node/mm^2 (f) 2630 node/mm^2

Figure 13. Influence of the number of particles on chip shape.

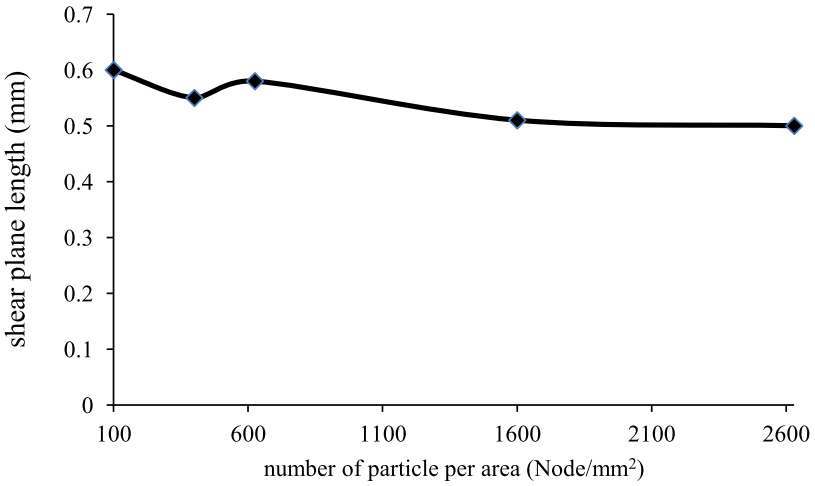

Figure 14. Influence of particle number on the shear plane length.

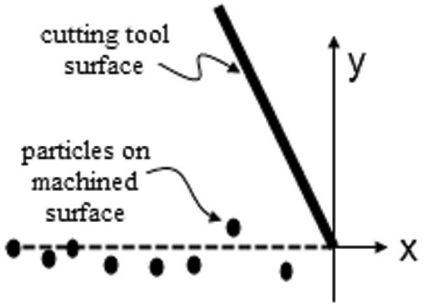

Figure 15. Particle position on the work-piece machined surface.

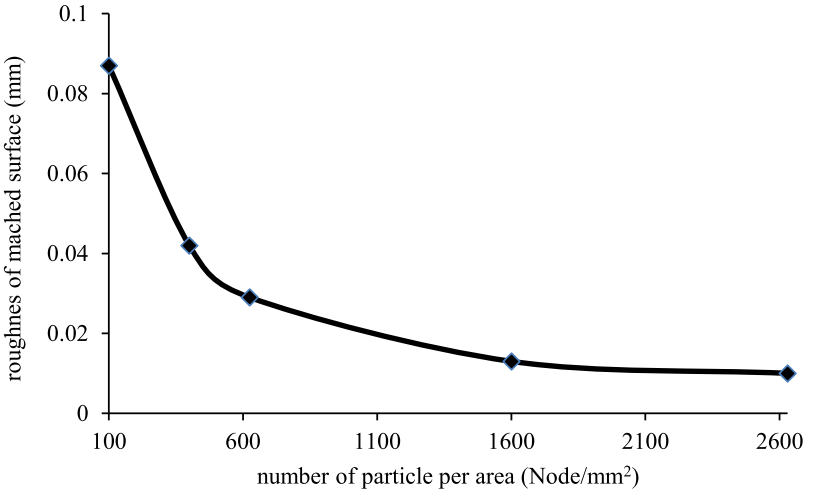

Figure 16. Influence of particle number on roughness of the work-piece machined surface.

Table 2. A Comparison of chip and shear plane length between the two algorithms presented in Figures 2 and 3

Work-piece material model	Return mapping algorithm (Figure 2)		The proposed algorithm (Figure 3)	
	Shear plane length (mm)	Chip length (mm)	Shear plane length (mm)	Chip length (mm)
EPP	0.53	1.17	0.51	1.2
JC	0.52	1.2	0.49	1.3

100, 400, 625, 1600 and 2630 node/mm^2 respectively. In the first case of Figure 13, due to the limited number of neighbours, the particles separate from each other and have a significant displacement in the vertical direction. The chip forms to its final shape by increasing number of particles. Particularly, the length of chip convergences by 400 (node/mm^2) and teeth of the chip are easier to detect with 1600 (node/mm^2).

The effect of ratio particle number per work-piece area on shear plane length and the machined work-piece surface at the back of the tool tip are investigated at Figures 14 and 16 respectively. The roughness of a surface is calculated using relation (27) based on Figure 15 where n is the number of particles on machined surface. In this study, the ratio 1600 (node/mm^2) is used to

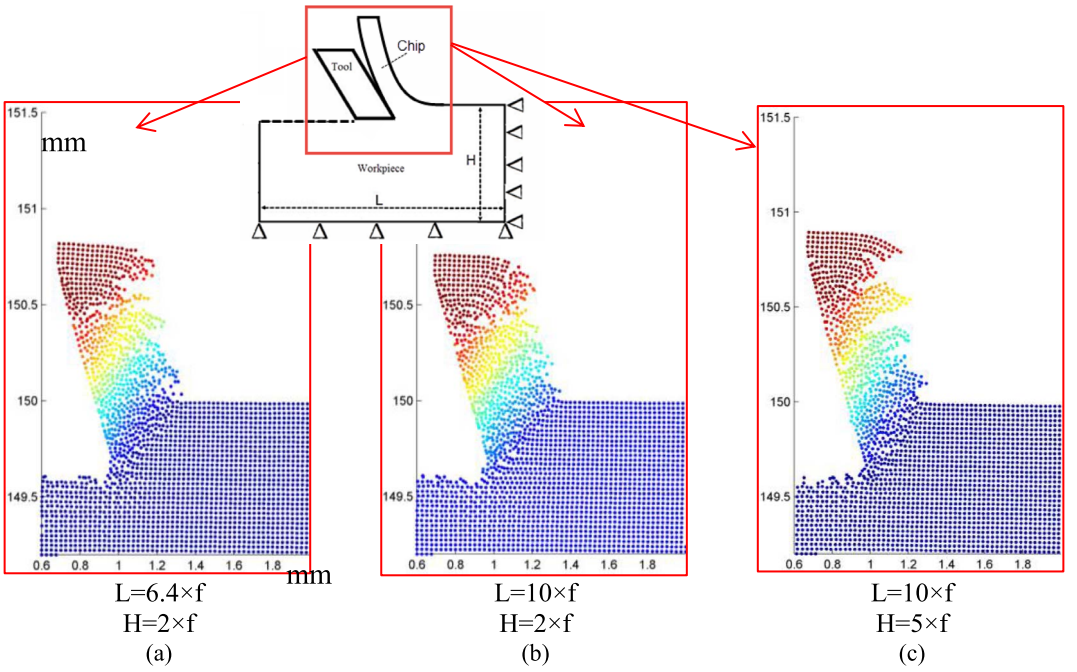

Figure 17. Influence of the work-piece dimensions on the chip shape.

model the work-piece based on Figures 14 and 16.

$$R = \frac{\sum_{i=1}^{n} |y_i|}{n} \tag{27}$$

Three work-pieces with various dimensions are analysed at Figure 17 to investigate the influence of $L \times H$ at Figure 6 on chip morphology using kinematic tool and EPP material model. The effect of supports on chip morphology decreases by increasing the distance between the supports and cutting tool tip or the work-piece dimensions. The work-piece area of Figure 17(b) and (c) is 1.6 and 3.9 times to the part (a). The advancements of cutting tools and the plotted area of parts of this figure are equalled.

According to Figure 17, three teeth are shaped and the fourth tooth is being formed. The first teeth are similar in all three cases. This similarity is due to the fact that the tool tip gap to the supports in all three cases is far enough and stress distribution in the work piece is more affected by the entering of the tool tip. Therefore, all three cases in Figure 17 experience practically identical conditions at the time of the first tooth formation. With the advancement of the tool tip, the contribution of the work-piece support in the stress distribution increases. The second and third teeth in parts of Figure 17 (a) and (b) are not completely formed due to the closeness of down support to the cutting area, but the tips of the teeth are clearly identified in the case (c). The chips formation are similar in all three cases based on the formation of the fourth tooth in this figure. At this time, the fourth tooth forms and rises on the shear plane. The chip thickness and the gap between the teeth are equal in all three parts. Chip (a) is very similar to the chip (c) and is economical due to the less area of the work-piece. In this paper, this model is used to analyse the orthogonal cutting process in various conditions.

The von Mises stress distribution in the work-piece is shown at Figure 18 at four different time periods of 0.005, 0.015, 0.05, and 0.65 milliseconds using kinematic tool and EPP material model.

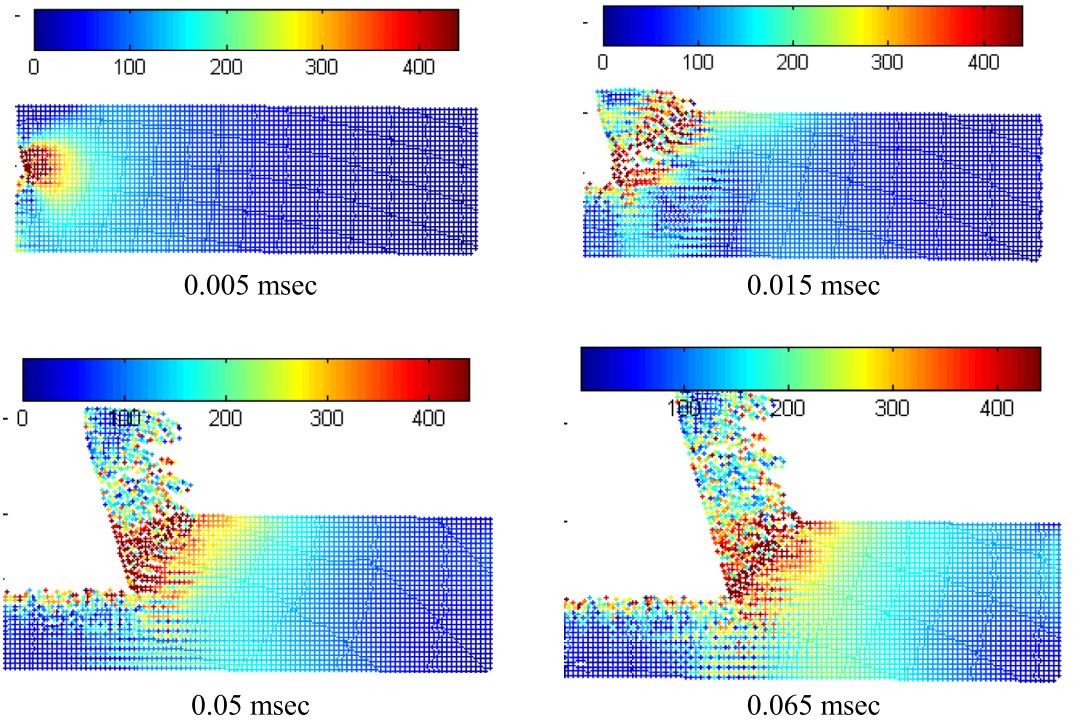

Figure 18. Analysing the von Mises stress distribution in the work-piece using kinematic tool and EPP material model at four different time periods of 0.005, 0.015, 0.05, and 0.65 milliseconds.

Time 0.005 msec relates to the entering of the cutting tool into the work-piece. At this moment, the stress at the right edge of work-piece is zero and near the tool tip is maximum. At the 0.015 msec, the first tooth is forming. The stress at the shear plane gets its maximum value and causes the formation of the shear plane. As the tool moves forward, the tooth moves on this plane to the outside of the work-piece. However, the stress at the right edge of work-piece is zero, because the distance between this support and tool tip is far enough.

The von Mises stress increases at the width of work-piece of Figure 18 by the movement of the tool tip near the right edge of the work-piece. At this time, the support effects on the shape of the chip. According to the variations of stress distribution in the work-piece, the shape of the chip is only influenced by the interaction of the cutting tool on the work-piece particles until the tool tip moves close to the half-length of the work-piece.

Figure 19 shows the cutting forces of the orthogonal cutting process with various rake angles and feed rates using kinematic tool and EPP material model and experimental result [24] are shown in this figure.

Based on Figure 19, the numerical cutting force is similar to the experimental result. The cutting force increases and decreases by increasing the feed rate and the rake angle respectively. The cutting force of the tool with a rake angle of 5, 10, and 17.5° vary 1.5, 1.5 and 1.67 times higher, respectively by increasing 0.1 mm/rev of the feed rate. The cutting force of the tool with a rake angle of 5° is 1.09 and 1.19 times to the cutting forces of the tool with rake angle 10° and 17.5° and feed rate of 0.4 mm/rev, respectively. These ratios are 1.09 and 1.34 for feed rate 0.3 mm/rev.

Comparisons between chip shapes of work-piece with two different material models (JC and EPP) are investigated at Figure 20 while feed rate is 0.4 mm/rev. The lengths of the chips, as well as

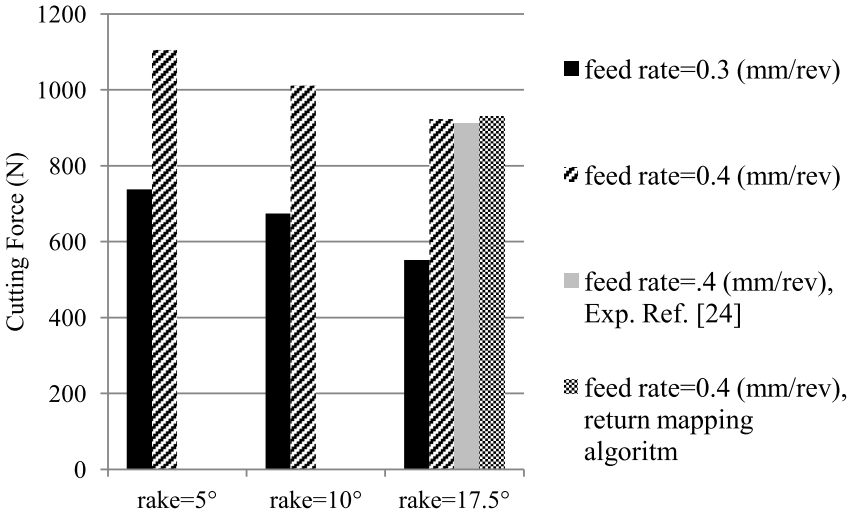

Figure 19. Comparing the cutting force of the orthogonal cutting process with the rake angle of 5, 10 and 17.5° and the feed rate of 0.3 and 0.4 mm/rev.

their thickness at the steady state process are the same for each rake angles. The cutting process remains steady state while the influence of the entering cutting tool reduces.

The variations of temperature distribution of the orthogonal cutting process are shown at Figure 21. In this analysis, the feed rate, rake angle and material model are 0.3 mm/rev, 17.5° and JC model respectively. This temperature distribution is based on the energy variation of particles as performing work and heat conduction. In this figure, the particles temperature increase with the separation from the shear plane. The particles on chip-tool interface at the feed rate region experience the high temperature variations, their temperatures decrease by getting away from the cutting tool tip. The maximum temperature increases from 80 °C to 100 °C during the formation of a new tooth at Figure 21(a) to (c). Then this temperature decreases at part (d) and this process is occurred repeatedly at parts (e) and (f).

The von Mises stress at the states of Figure 21 are shown at Figure 22. Based on Figure 22, the maximum von-Mises stress is at the cutting surface. The maximum von Mises stress as the maximum temperature rises at parts (a) to (d) during the formation of a tooth and this process starts repeatedly at part (e).

The maximum von Mises stress is 600 MPa at Figure 22, but this is 440 MPa at the Figure 18, because the yield stress of EPP material model is constant but JC yield stress varies by temperature, plastic strain and plastic strain rate.

An initially regular particle distribution at the work-piece at all previous results is used. Six different work-piece particle distributions of Figure 23 are used to show the influence of the particle alignment on the particle displacements and von Mises stress. According to Figures 24 and 25 the particle displacement and von Mises stress of initially regular and irregular particle distribution at the work-piece approximately are the same.

In all previous results, it is assumed that the tool tip radius (r at Figure 26) is zero. The work-piece variations at the entering time of the tool with tip radius 0.15, 0.12, 0.08, 0.04 and 0.02 mm are plotted at Figure 27. The feed rate and cutting speed of this analysing are 0.4 mm/rev and 800 m/min respectively using kinematic tool and the JC material model.

Based on Figure 27, the left work-piece boundary coincides with the tool tip curvature. The upper boundary displacement increases by increasing tool tip radius. A tool with small tip radius

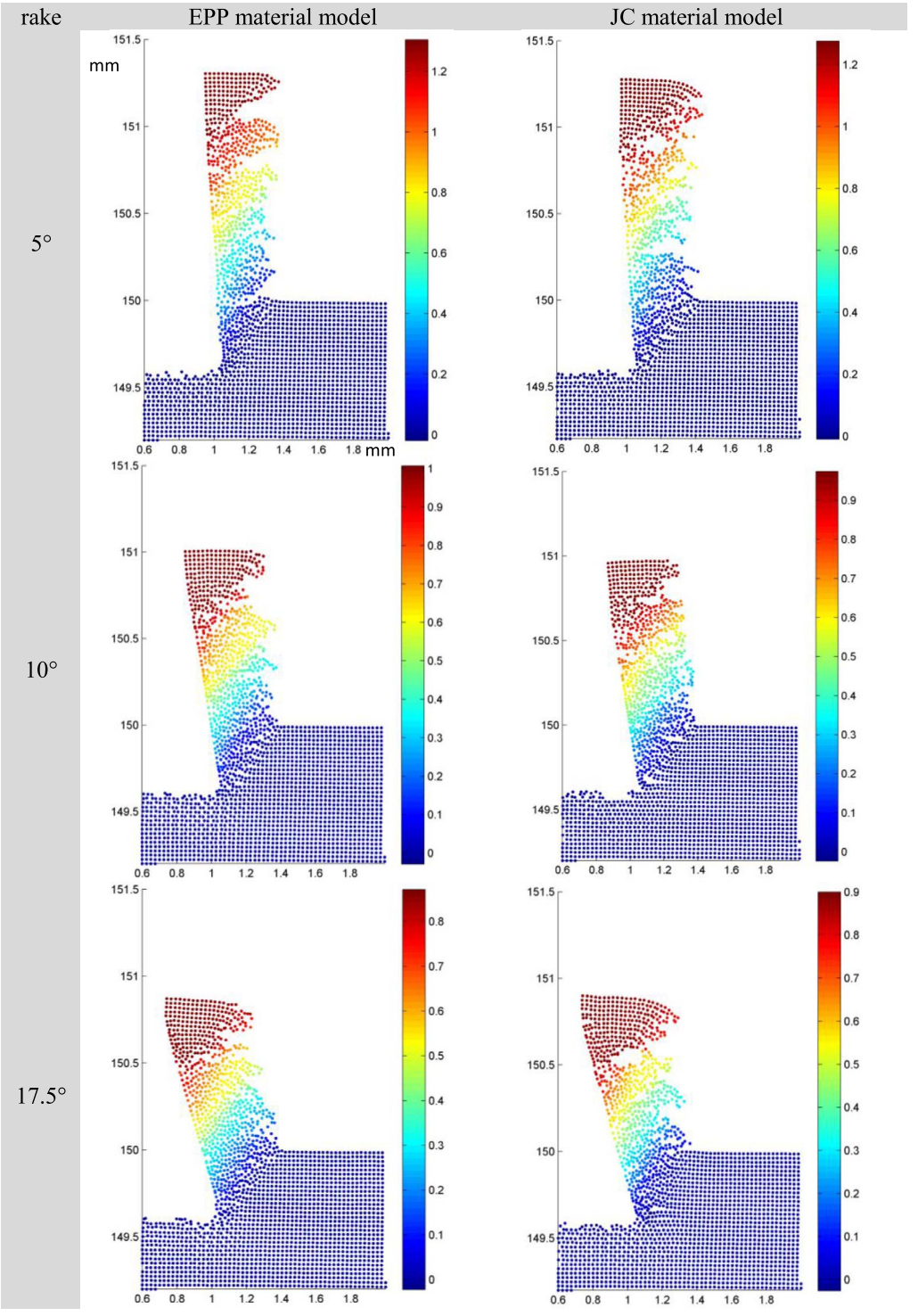

Figure 20. Comparisons between chip shape of work-piece with two different material models JC and EPP are investigated. The rake angles are 5, 10, and 17.5 and feed rate is 0.4 mm/rev.

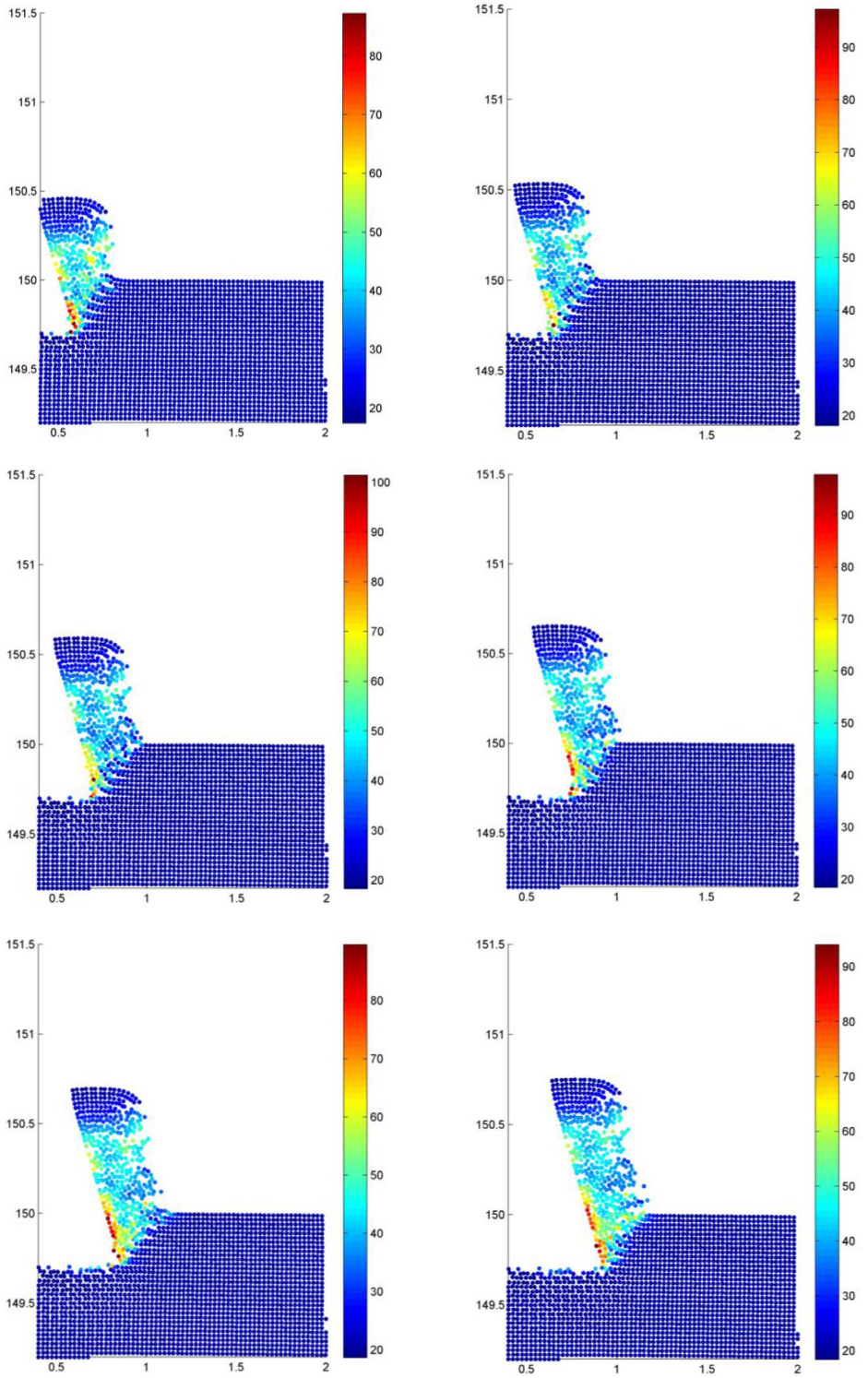

Figure 21. Investigating temperature variations during the formation of a tooth using kinematic tool and JC material model.

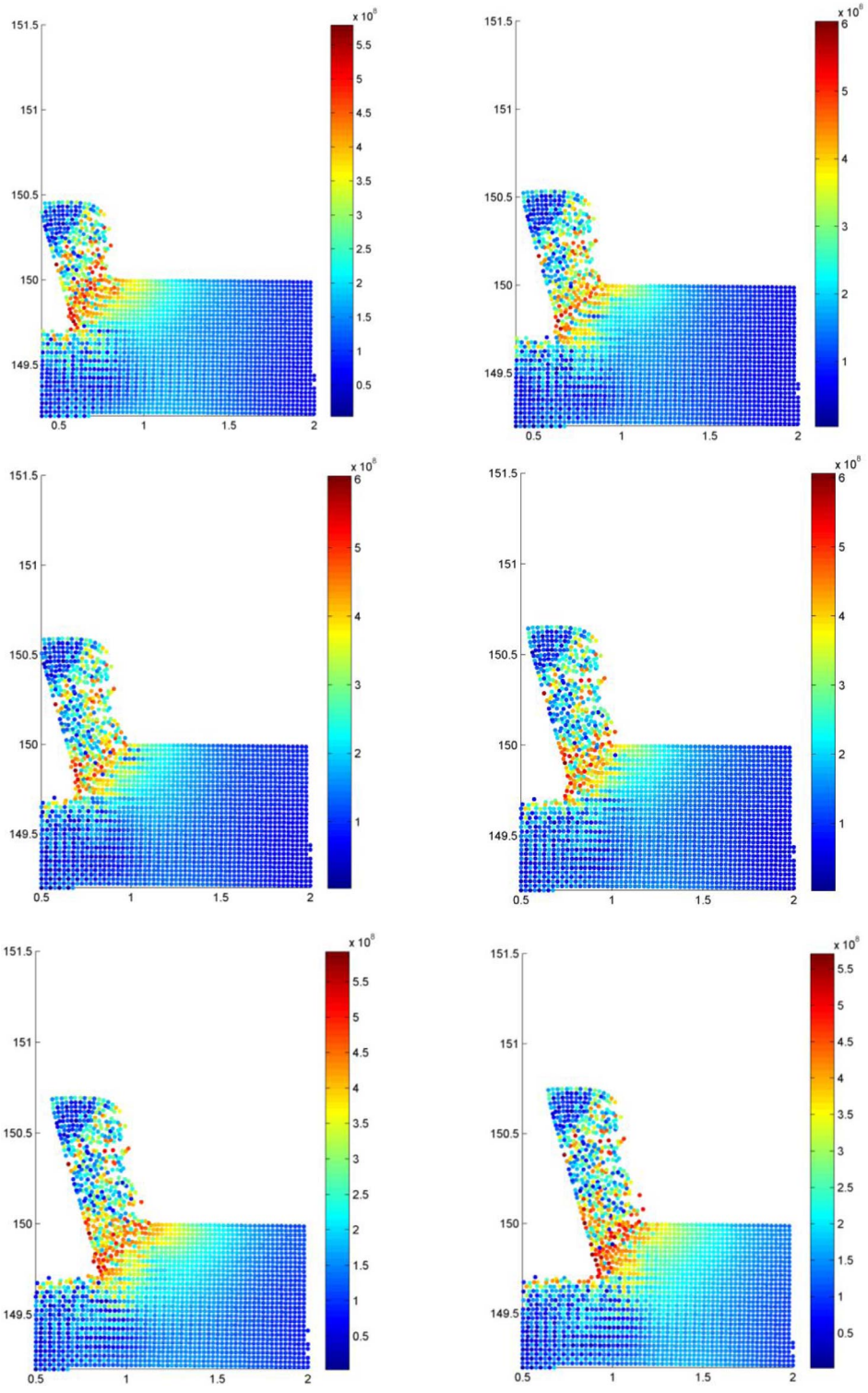

Figure 22. Variation of von Mises stress during the formation of a tooth.

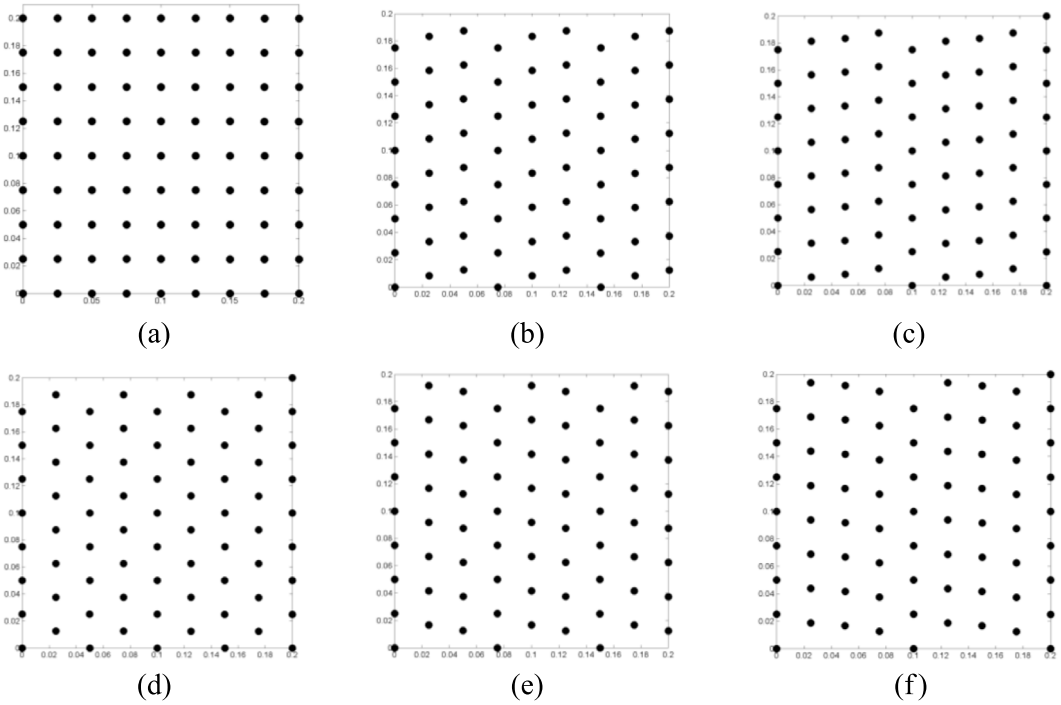

Figure 23. Initially (a) regular and (b–f) irregular particle distribution at the work-piece.

cuts the left boundary however tool with big tip radius changes the vertical position of this boundary but it doesn't cut it.

Figure 28 shows the chip shape of the orthogonal cutting process with various tool tip radius. Varying chip direction on a rake face with a big tip radius causes teeth separating from each other. Therefore; the length of the chip increases by increasing the tool tip radius.

5. Conclusion

In this investigation, the cutting process is assumed to be a two-dimensional orthogonal cutting process in which the cutting speed is perpendicular to the cutting depth. The work-piece of the orthogonal cutting process is analysed using smooth particle hydrodynamic (SPH) method. The material is divided into SPH particles. The particle model can model the large deformations and ruptures of the work-piece. Normal and friction force at the traditional kinetic model of the cutting tool and the work-piece particles interface is replaced with kinematic reactions. In kinetic model, the coefficient of friction between cutting tool and the work-piece affects the results such as the cutting force and chip shape. In kinematic model, the horizontal component velocities of work-piece particles are varied to the cutting speed while those are placed at the cutting tool region.

The constitutive work-piece material model is assumed as the elastic-perfectly plastic material model. The yield stress of this material model is constant or varies by Johnson–Cook model based on variations of temperature, plastic strain and plastic strain rate.

The chip shape of experimental orthogonal cutting process was compared with the results of the SPH method with the kinetic/kinematic cutting tool including two material models: EPP and JC model. Furthermore, the chip shape of reference [26] is added to this comparison

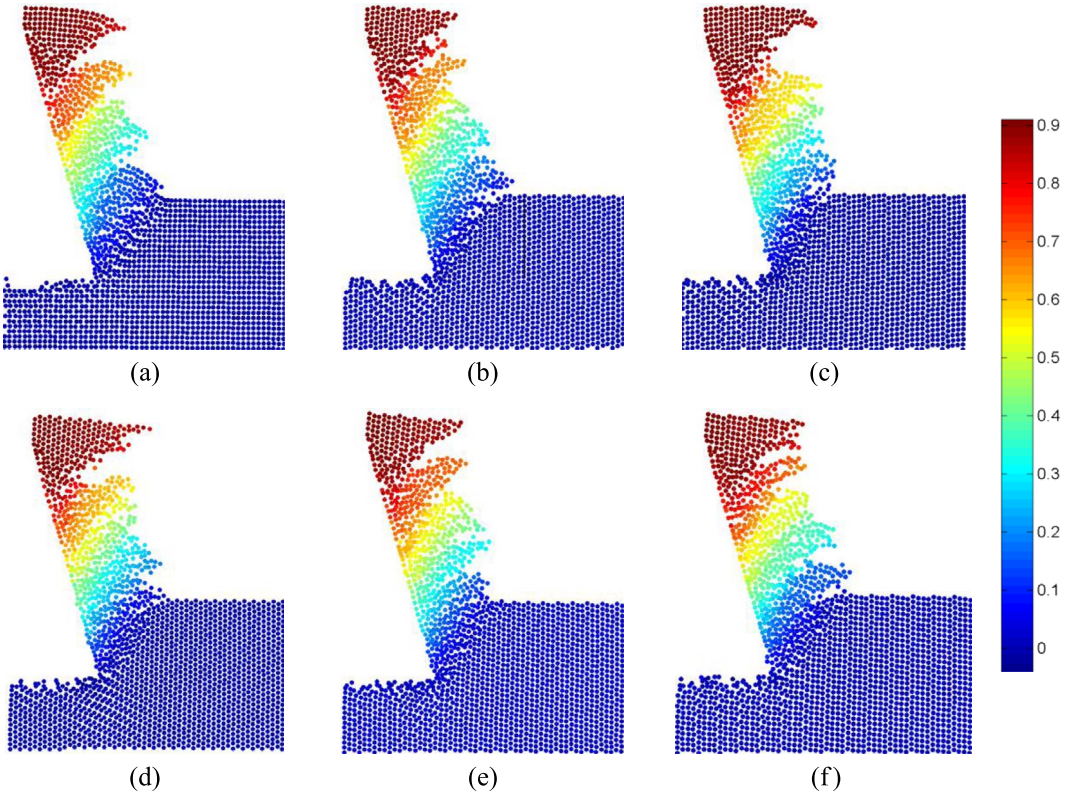

Figure 24. Influence of the alignment of the particles on displacement along perpendicular to the cutting speed due to the initially (a) regular and (b–f) irregular particle distribution at the work-piece.

used the kinetic tool. The chip of cutting simulation with the kinematic tool is more similar to experimental results while the cutting speed, rake angle and feed rate are 60 m/min, 15° and 0.3 mm/rev respectively.

Various work-piece cases are studied to investigate the influence of the work-piece dimensions on chip morphology. A work-piece model at Figure 6 with $H = 2 \times f$ and $L = 6.4 \times f$ can be used to simulate an orthogonal cutting process. By this dimensions, the influence of work-piece boundaries on stress distribution decreases while the cutting tool advances to the half of work-piece length.

The comparison between chip shapes of work-piece with two material models were investigated those included various rake angles 5, 10 and 17.5° and feed rates 0.3 and 0.4 mm/rev. The length and thickness of the chips of these two material models are similar. This similarity increases by raising the rake angle and feed rate.

The cutting force of cutting process with 5, 10, 17.5° tool rake angles and 0.3, 0.4 mm/rev feed rate are obtained. The cutting force of the process with 17.5° rake angle and 0.4 mm/rev feed rate is validated using experimental result.

Approximately initial work-piece particle distributions don't influence on the particle displacements and von Mises stress.

Varying chip direction on a rake face with a big tip radius causes gap creation between the teeth. Therefore; the length of chip increases by increasing the tool tip radius.

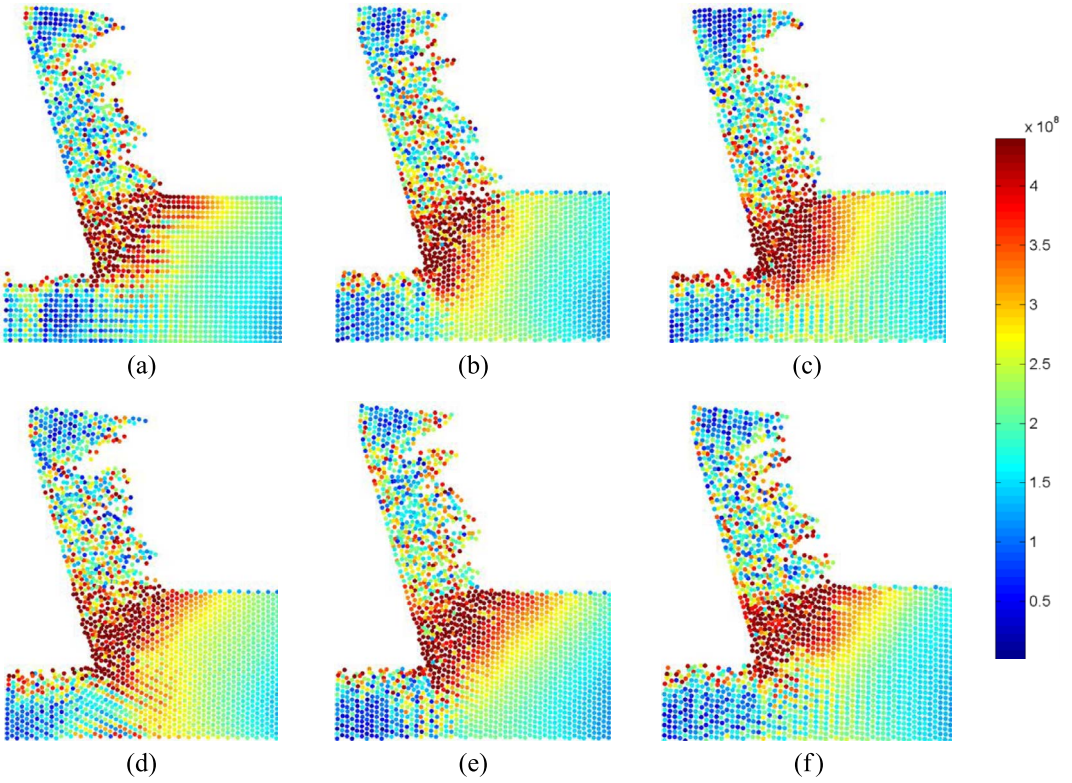

Figure 25. Influence of the alignment of the particles on von Mises stress due to the initially (a) regular and (b–f) irregular particle distribution at the work-piece.

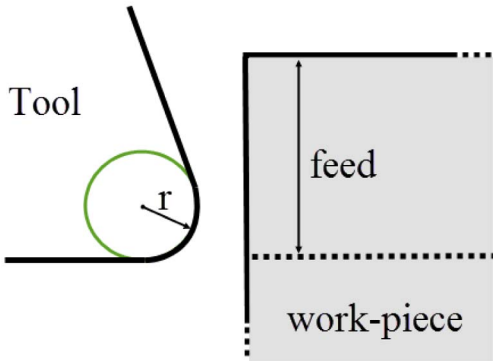

Figure 26. The tool tip radius (r).

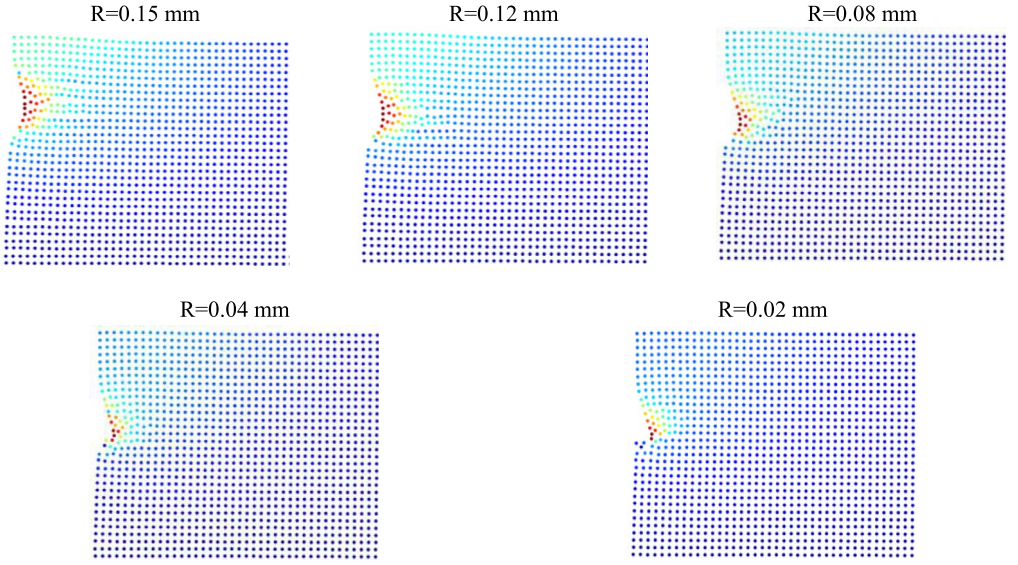

Figure 27. Influence of tool tip radius on work-piece at the beginning of the cutting process.

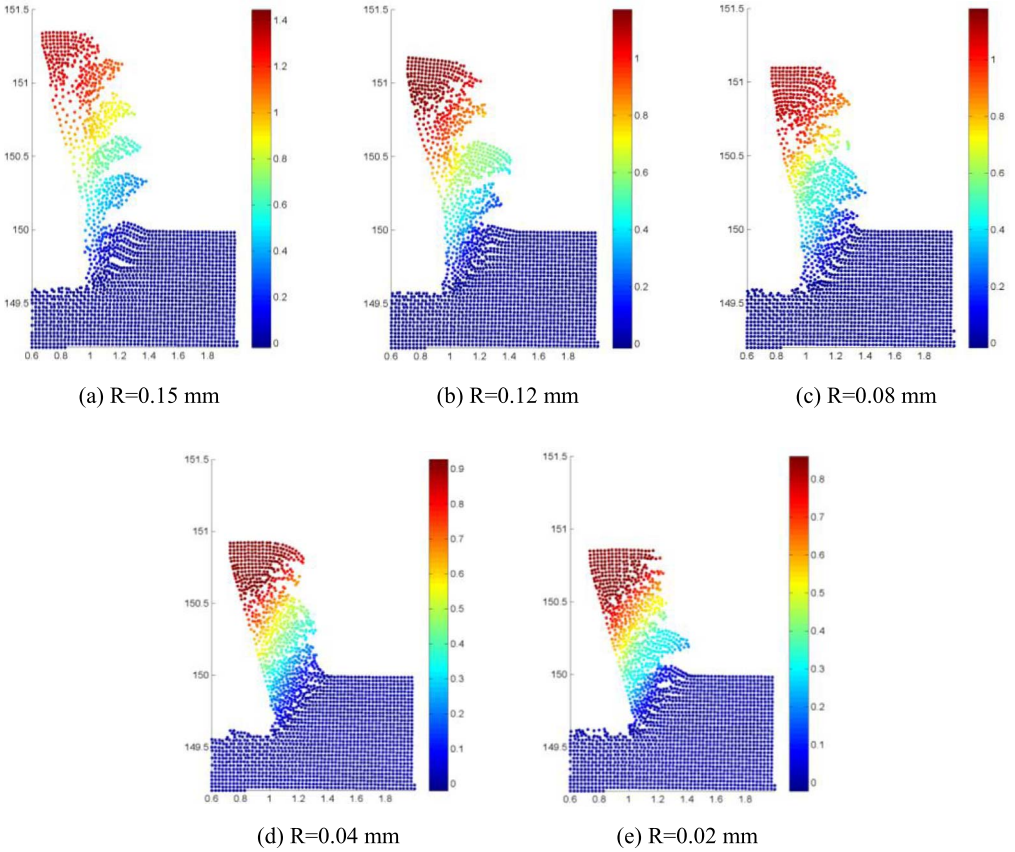

(a) R=0.15 mm (b) R=0.12 mm (c) R=0.08 mm

(d) R=0.04 mm (e) R=0.02 mm

Figure 28. Influence of tool tip radius on chip shape.

References

[1] E. Budak, E. Ozlu, "Development of a thermomechanical cutting process model for machining process simulations", *CIRP Ann. - Manuf. Technol.* **57** (2008), p. 97-100.

[2] S. N. Melkote, W. Grzesik, J. Outeiro, J. Rech, V. Schulze, H. Attia, P. Arrazola, R. M. Saoubi, C. Saldana, "Advances in material and friction data for modelling of metal machining", *CIRP Ann. - Manuf. Technol.* **66** (2017), p. 731-754.

[3] W. Bai, R. Sun, A. Roy, V. V. Silberschmidt, "Improved analytical prediction of chip formation in orthogonal cutting of titanium alloy Ti6Al4V", *Int. J. Mech. Sci.* **133** (2017), p. 357-367.

[4] K. Yamaguchi, M. Yamada, "Stress distribution at the interface between tool and chip in machining", *J. Eng. Ind.-Trans. ASME* **94** (1972), p. 683-689.

[5] E. Trent, P. Wright, *Metal Cutting*, 4th ed., Elsevier, 2000.

[6] C. Zhang, J. Lu, F. Zhang, S. Ikramullah, "Identification of a new friction model at tool-chip interface in dry orthogonal cutting", *Int. J. Adv. Manuf. Technol.* **89** (2017), p. 921-932.

[7] E. Cakir, E. Ozlu, M. Bakkal, E. Budak, "Investigation of temperature distribution in orthogonal cutting through dual-zone contact model on the rake face", *Int. J. Adv. Manuf. Technol.* **96** (2018), p. 81-89.

[8] M. Asad, F. Girardin, T. Mabrouki, J.-F. Rigal, "Dry cutting study of an aluminium alloy (A2024-T351): a numerical and experimental approach", *Int. J. Mater. Form.* **1** (2008), p. 499-502.

[9] M. Calamaz, D. Coupard, F. Girot, "A new material model for 2D numerical simulation of serrated chip formation when machining titanium alloy Ti – 6Al – 4V", *Int. J. Mach. Tools Manuf.* **48** (2008), p. 275-288.

[10] C. Maranhão, J. P. Davim, "Simulation modelling practice and theory finite element modelling of machining of AISI 316 steel: Numerical simulation and experimental validation", *Simul. Model. Pract. Theory* **18** (2010), p. 139-156.

[11] L. Tang, J. Huang, L. Xie, "Finite element modeling and simulation in dry hard orthogonal cutting AISI D2 tool steel with CBN cutting tool", *Int. J. Adv. Manuf. Technol.* **53** (2011), p. 1167-1181.

[12] L. Wan, B. Haddag, D. Wang, Y. Sheng, D. Yang, "Effects of friction conditions on the formation of dead metal zone in orthogonal cutting – a finite element study", *Mach. Sci. Technol.* (2018), p. 934-952.

[13] P. L. Menezes, I. V. Avdeev, M. R. Lovell, C. F. H. Iii, "An explicit finite element model to study the influence of rake angle and friction during orthogonal metal cutting", *Int. J. Adv. Manuf. Technol.* **73** (2014), p. 875-885.

[14] F. Ducobu, E. Filippi, "On the introduction of adaptive mass scaling in a finite element model of Ti6Al4V orthogonal cutting", *Stimul. Model. Pract. Theory* **53** (2015), p. 1-14.

[15] F. Ducobu, E. Filippi, "Finite element modelling of 3D orthogonal cutting experimental tests with the Coupled Eulerian-Lagrangian (CEL) formulation", *Finite Elem. Anal. Des.* **134** (2017), p. 27-40.

[16] E. Filippi, F. Ducobu, E. Rivi, "Mesh influence in orthogonal cutting modelling with the Coupled Eulerian-Lagrangian (CEL) method", *Eur. J. Mech. A / Solids* **65** (2017), p. 324-335.

[17] W. Jomaa, O. Mechri, J. Lévesque, V. Songmene, "Finite element simulation and analysis of serrated chip formation during high – speed machining of AA7075 – T651 alloy", *J. Manuf. Process.* **26** (2017), p. 446-458.

[18] S. Usui, J. Wadell, T. Marusich, "Finite element modeling of carbon fiber composite orthogonal cutting and drilling", in *6th CIRP Int. Conf. High Perform. Cutting, HPC2014*, Elsevier B.V., 2014, p. 211-216.

[19] S. P. F. C. Jaspers, J. H. Dautzenberg, D. A. Taminiau, "Temperature measurement in orthogonai metal cutting", *Int. J. Adv. Manuf. Technol.* **14** (1998), p. 7-12.

[20] X. Y. Gu, C. Y. Dong, T. Cheng, "MPM simulations of high-speed machining of Ti6Al4V titanium alloy considering dynamic recrystallization phenomenon and thermal conductivity", *Appl. Math. Modelling* **56** (2018), p. 517-538.

[21] X. Geng, W. Dou, J. Deng, F. Ji, Z. Yue, "Simulation of the orthogonal cutting of OFHC copper based on the smoothed particle hydrodynamics method", *Int. J. Adv. Manuf. Technol.* **91** (2017), p. 265-272.

[22] J. Nam, T. Kim, S. W. Cho, "A numerical cutting model for brittle materials using smooth particle hydrodynamics", *Int. J. Adv. Manuf. Technol.* **82** (2016), p. 133-141.

[23] C. S. Avachat, N. Carolina, N. Carolina, "A parametric study of the modeling of orthogonal machining", in *Proc. ASME 2015 Int. Mech. Eng. Congr. Expo.*, American Society of Mechanical Engineers Digital Collection, 2015, p. 1-10.

[24] M. Madaj, M. Píška, "On the SPH orthogonal cutting simulation of A2024-T351 alloy", *Procedia CIRP* **8** (2013), p. 152-157.

[25] LS-DYNA Keyword User's Manual, 2007.

[26] W. Niu, R. Mo, G. R. Liu, H. Sun, X. Dong, "Modeling of orthogonal cutting process of A2024-T351 with an improved SPH method", *Int. J. Adv. Manuf. Technol.* **95** (2018), p. 905-919.

[27] G. R. Liu, M. B. Liu, *Smooth Particle Hydrodynamics: A Mesh Free Particle Method*, World Scientific, 5 Toh Tuck Link, Singapore, 2003, ISBN 9789812384560.

[28] N. H. Kim, D. R. J. Owen, *Introduction to Nonlinear Finite Element Analysis*, Springer, Department of Mechanical and Aerospace Engineering, University of Florida, Gainesville, FL, USA, 2015.

[29] J. D. Seidt, A. Gilat, "Plastic deformation of A2024-T351 aluminum plate over a wide range of loading conditions", *Int. J. Solids Struct.* **50** (2013), p. 1781-1790.

[30] E. A. Patiño, R. Reyes, D. A. García, A. F. Sarmiento, J. M. Arroyo, D. A. Garzon, "Implementation of the smoothed particle hydrodynamics method to solve plastic deformation in metals", in *10th World Congr. Comput. Mech.*, Blucher Mechanical Engineering Proceedings, 2014.

[31] B. Haddag, S. Atlati, M. Nouari, "Dry machining aeronautical aluminum alloy AA2024-T351: Analysis of cutting forces, chip segmentation and built-up edge formation", *Metals (Basel)* **6** (2016), p. 197.